Neutron-rich fragments produced by in-flight fission of ^{238}U

D. Pérez-Loureiro,[1,*] J. Benlliure,[1,†] J. Díaz-Cortes,[1] J. L. Rodríguez-Sánchez,[1] H. Álvarez-Pol,[1] B. Blank,[2] E. Casarejos,[3] D. Dragosavac,[1] V. Föhr,[4] M. Gascón,[1] W. Gawlikowicz,[5] A. Heinz,[6] K. Helariutta,[7] A. Kelić-Heil,[4] S. Lukić,[4] F. Montes,[4,‡] L. Pieńkowski,[8] K-H. Schmidt,[4] M. Staniou,[4] K. Subotić,[9] K. Sümmerer,[4] J. Taieb,[10] and A. Trzcińska[8]

[1]*IGFAE, Universidade de Santiago de Compostela, E-15782 Santiago de Compostela, Spain*
[2]*Centre d'Etudes Nucleaires, F-33175 Bordeaux-Gradignan Cedex, France*
[3]*Universidad de Vigo, E-36310 Vigo, Spain*
[4]*GSI Helmholtzzentrum für Schwerionenforschung GmbH, D-64291 Darmstadt, Germany*
[5]*Cardinal Stefan Wyszyski University, Warsaw, Poland*
[6]*Chalmers University of Technology, SE-41296 Gothenburg, Sweden*
[7]*University of Helsinki, FI-00014 Helsinki, Finland*
[8]*Heavy Ion Laboratory, University of Warsaw, PL-02-093 Warsaw, Poland*
[9]*Institute of Nuclear Sciences Vinča, University of Belgrade, 11001 Belgrade, Serbia*
[10]*CEA, DAM, DIF, F-91297 Arpajon, France*

(Received 26 December 2018; revised manuscript received 14 March 2019; published 6 May 2019)

The production cross sections of neutron-rich fission residues in reactions induced by ^{238}U projectiles at 950*A* MeV impinging on Pb and Be targets are investigated at the Fragment Separator at GSI. These two targets allow us to investigate fission processes induced by two reaction mechanisms, Coulomb and nuclear excitations, and to study the role of these mechanisms in the neutron excess of the final fragments.

DOI: 10.1103/PhysRevC.99.054606

I. INTRODUCTION

Medium-mass neutron-rich nuclei belong to one of the most exciting regions of the chart of nuclei because of their implications not only for nuclear structure studies, but also for stellar nucleosynthesis. The presence of several shell closures at large neutron excess ($Z = 28$, $N = 50$ and $Z = 50$, $N = 82$) provides an excellent basis for investigating how nuclear structure evolves with isospin [1]. Moreover, two of these shells ($Z = 50$, $N = 82$) are also at the origin of the waiting point at $A \approx 140$ in stellar r-process nucleosynthesis. Therefore, the production and study of nuclei in that region of the chart of nuclides are of utmost importance and have become a challenge for next-generation radioactive-beam facilities.

Although the fragmentation of neutron-rich beams, like ^{136}Xe, can produce some of the nuclei of interest [2], fission has been proven to be the most efficient mechanism for the production of medium-mass neutron-rich nuclei [3–10]. Indeed, all next-generation radioactive-beam facilities based on either isotope separation online (ISOL) or in-flight separation techniques use the fission of ^{238}U or ^{235}U to populate this region of the chart of nuclides. Furthermore, the EURISOL project [11] proposes a two-step reaction scheme where neutron-rich fission residues would be reaccelerated and fragmented to produce medium-mass nuclei with an even larger neutron excess [12,13].

In-flight fission at relativistic energies has clear advantages for the production of medium-mass neutron-rich secondary beams. This technique is not only applicable to any residual nucleus, regardless of its chemical properties, but also a very fast process giving access to extremely short-lived nuclei. The main drawbacks are related to the limited intensities of ion beams and the thicknesses of the target materials. Moreover, there is not much freedom concerning the reaction mechanism. Indeed, variations within certain limits in the projectile energy are not too relevant for the final production rates.

The choice of the target can, however, have an impact on the production of the final residual nuclei. In particular, the atomic number of the target material can be used to enhance either nuclear or Coulomb excitations. It is well established that the Coulomb interaction of ^{238}U projectiles with a high-Z target, like lead, may induce fission via excitation of the giant-dipole resonance. In this case, the excitation energy gained by the fissioning ^{238}U nuclei covers the range between 10 and 25 MeV, with a dominant peak at around 15 MeV. At those relatively low energies, fission is expected to produce an asymmetric fragment mass distribution [14]. Conversely, a low-Z target will enhance fragmentation-induced fission where the abrasion process will lead to a large variety of fissioning nuclei with excitation energies well above 20 MeV [15]. Under these conditions, the fission process will produce a symmetric mass distribution of fragments with a smaller neutron excess because of neutron evaporation.

It is the aim of this work to investigate the role of the target material in producing the largest variety of fission fragments with the largest possible neutron excess using in-flight fission of ^{238}U. This topic has been addressed by performing an

*Canadian Nuclear Laboratories Ltd., Chalk River Laboratories, Chalk River, Ontario K0J 1P0, Canada.
†j.benlliure@usc.es
‡NSCL-MSU, 1 Cyclotron, East Lansing, Michigan 48824, USA.

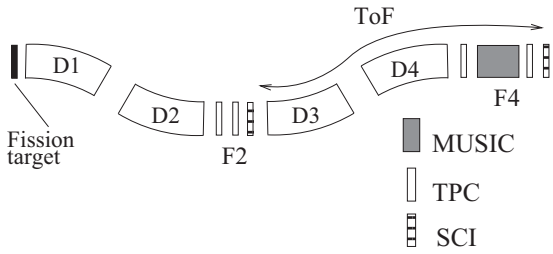

FIG. 1. Schematic of the FRS showing the dipole magnetic elements and the detection system used in the experiment. More details are given in the text.

experiment where the fragments produced in the fission of ^{238}U were fully identified by mass and atomic number taking advantage of the inverse kinematics technique. The role of the target material was investigated using two different targets, namely, lead and beryllium, enhancing Coulomb-induced fission at low excitation energies and nuclear-induced fission at higher excitation energies, respectively.

II. THE EXPERIMENT

The experiment was performed using the GSI accelerator facilities in Darmstadt. A beam of ^{238}U was accelerated by the SIS18 synchrotron to 950A MeV. The beam was then transported to the Fragment Separator (FRS) target station, where fission reactions were induced. The fission residues, focused in the forward direction, were analyzed by the zero-degree magnetic spectrometer FRS [16]. This is a two-stage achromatic spectrometer with a resolving power of $B\rho/\Delta B\rho \approx 1500$, a momentum acceptance of 1.5%, and an angular acceptance for the central trajectory of 15 mrad (see Fig. 1).

The A/Z ratio of the different fission fragments was unambiguously determined from their magnetic rigidity ($B\rho$) and velocity ($\beta\gamma$) according to the following relation:

$$B\rho \propto \frac{A}{Z}\beta\gamma. \quad (1)$$

An additional determination of the corresponding atomic number using energy loss measurements provided unambiguous identification of the fragments by atomic and mass number. A detailed description of the experimental technique and analysis procedure can be found in Ref. [17].

During the experiment the beam intensity was continuously monitored with the secondary-electron current monitor SEETRAM [18]. The intensity of the ^{238}U ions ranged from 10^7 ions/s up to 5×10^8 ions/s. The two targets used in this experiment had a thickness of 1036 mg/cm^2 for beryllium and 649 mg/cm^2 for lead. The FRS was equipped with detection systems adequate to provide identification of the transmitted nuclei. Time-projection chambers (TPCs in Fig. 1) placed at both image planes of the spectrometer (F2 and F4 in Fig. 1) were used to determine the position of the transmitted nuclei along the dispersive coordinate. These positions, together with the dispersion and magnification parameters of the spectrometer, provided the magnetic rigidity $B\rho$ of each nucleus. Two fast plastic scintillators (SCIs in Fig. 1) covering the full

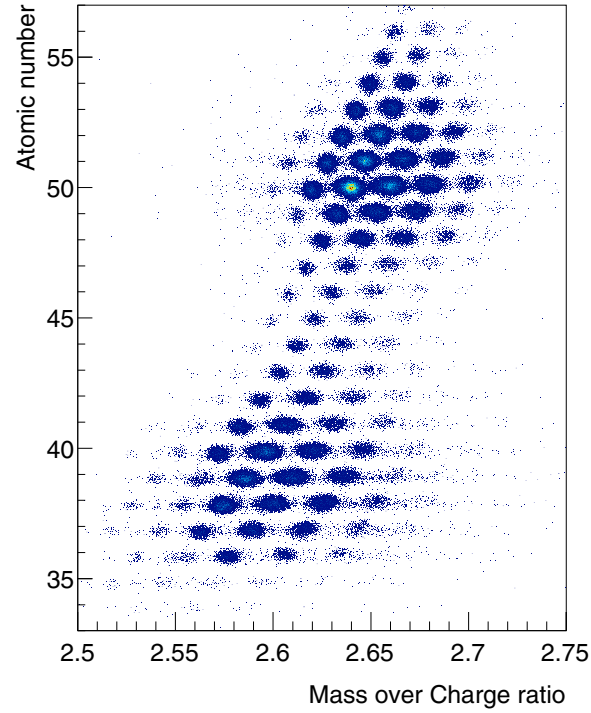

FIG. 2. Two-dimensional scatterplot representing the atomic number of the fission fragments versus their A/Z value for a setting of the FRS centered on ^{135}Sn with the lead target. The color scale indicates the production yield.

acceptance, also at both image planes, were used to measure the time of flight and, accordingly, the velocity $\beta\gamma$ of each nucleus. Finally, a fast ionization chamber (MUSIC in Fig. 1) situated on the final image plane provided the measurement of the energy loss of the fragments with a resolution sufficient to determine their atomic number Z. By combining the measurements of the magnetic rigidity, velocity, and energy loss it was possible to separate and identify all the fragments transmitted through the FRS according to their atomic and mass numbers. The calibration of atomic and mass number was obtained from the characteristic pattern of the distribution of fission fragments produced at low energies, as induced by the lead target in the present experiment, together with ion-optical calculations predicting the corresponding positions of the transmitted nuclei on the final image plane of the spectrometer.

Figure 2 shows the identification matrix of the fission residues produced in the reaction ^{238}U + Pb at 950A MeV that reach the final focal plane of the FRS for a magnetic setting centered on ^{135}Sn. The excellent resolving power of the spectrometer made it possible to separate and identify unambiguously the fission fragments produced in the investigated reactions. In order to cover the production of the most neutron-rich fragments produced in fission within the angular acceptance of the FRS, four different magnetic tunings of the FRS, centered on ^{129}Sn, ^{132}Sn, ^{135}Sn, and ^{138}Sn, were used. As discussed in the following, by overlapping the measured production of each nucleus over consecutive magnetic tunings

we could determine the production yields and then the cross sections.

III. RESULTS

A. Production cross sections

The cross sections of the most neutron-rich fission fragments produced in reactions induced by ^{238}U projectiles impinging upon beryllium and lead targets were determined from the production yields of each nucleus $Y(A, Z)$, normalized to the number of projectiles N_p and the number of atoms per unit area in the target N_t, according to the following equation:

$$\sigma(Z, A) = \frac{\epsilon Y(Z, A)}{N_p N_t}. \quad (2)$$

The number of impinging projectiles was directly determined from the beam monitor, and the atoms per unit area in the target from the known target thickness. The production yield of each fragment was obtained from the identification matrices, measured on the final focal plane of the spectrometer. These yields were corrected by a factor ϵ accounting for the different losses incurred by the experimental setup. This factor not only includes the detection efficiency, the optical transmission through the spectrometer, or the data acquisition dead time, but also the probability of having multiple reactions in the target or secondary reactions of the final fragments in the different layers of matter placed along the spectrometer.

The overall detection efficiency of the detectors used in this experiment varied between 85% and 97%, depending on the atomic number of the ions, and the dead time of the data acquisition was continuously monitored, with values below 30%. Due to the limited acceptance of the fragment separator and the large spread of fission fragments in both angle and momentum, only forward-emitted fragments were measured. For these fragments the complete velocity distribution was determined by summing the different contributions measured in consecutive magnetic tunings of the FRS. The angular transmission of the fission fragments was evaluated according to the method proposed in Ref. [19], ranging from 40% for the heaviest fragments down to 10% for the lightest ones. The probability for secondary reactions in other layers of matter traversed by the ions was evaluated with the Karol formula [20] and the probability for multiple reactions in the target following the method presented in Ref. [21]. The combined correction due to these two effects was between 20% and 30%.

The precision of these measurements was mainly limited by systematic uncertainties; only for the most neutron-rich nuclei with the lowest cross sections were Poisson statistics the main source of uncertainty. Most of the systematic uncertainties were below 10% and only the one associated with the optical transmission was of the order of 20%.

Figure 3 displays cluster plots with the production cross sections measured for the lead target (upper panel; 178 fission fragments) and for the beryllium target (lower panel; 330 fission fragments). In both cases, the plots have been superimposed upon the corresponding region of the chart of nuclides. As can be seen, with both measurements we could investigate the production of very neutron-rich fission fragments of elements from krypton up to neodymium, with the lead target, and from gallium to cerium, with the beryllium one. The isotopic distributions of these elements covers the range from the most abundant isotopes in fission to more neutron-rich isotopes with cross sections as low as 100 pb.

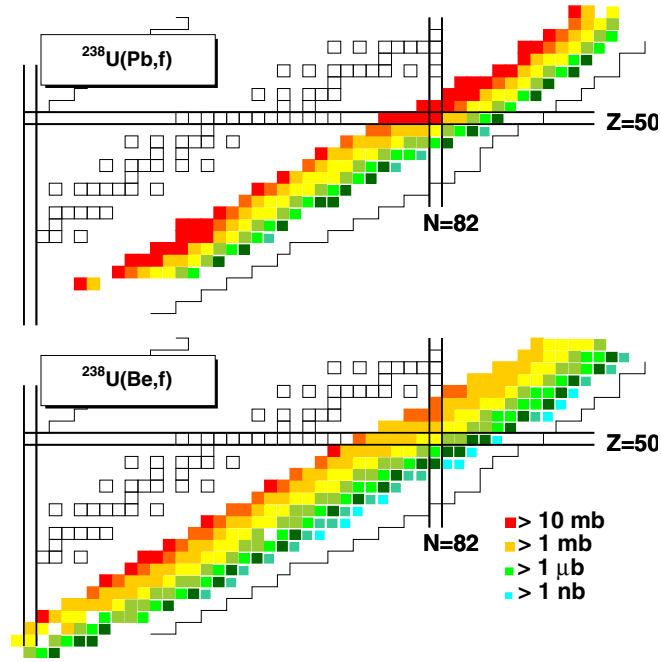

FIG. 3. Fission fragments measured in this work, with the lead (upper panel) and beryllium (lower panel) targets superimposed on two charts of nuclides. The color code and cluster size indicate the production cross sections.

B. Fission induced by the lead target

In Fig. 4 we present the isotopic distributions of the fission fragments measured in this work with the lead target (solid points). We also show fission data previously obtained by Enqvist *et al.* (open circles) for the same reaction at a slightly higher energy, 1000*A* MeV, but using also the FRS with a very similar detection setup [22]. As can be seen, both sets of data not only overlap within uncertainties but also are fully complementary. Enqvist *et al.* measured long isotopic chains of fission residual nuclei produced in the reaction ^{238}U + Pb, but they could not reach the most neutron-rich fragments. However, the new data extend over the region of fission fragments with a larger neutron excess and smaller production cross sections.

The two data sets fully cover the region of fission, with production yields following the typical behavior of low-energy fission. The fragment distribution is clearly asymmetric in neutron and atomic number as shown in the upper panels in Fig. 3 and in Fig. 4. In these figures we observe the highest production yields for nuclei around ^{134}Te and ^{142}Xe, corresponding to the spherical shell at $N \approx 82$ and the deformed one at $N \approx 88$, and their complementary fragments ^{104}Zr and ^{96}Sr [23]. Moreover, the region around the symmetric splitting presents much lower production yields. This

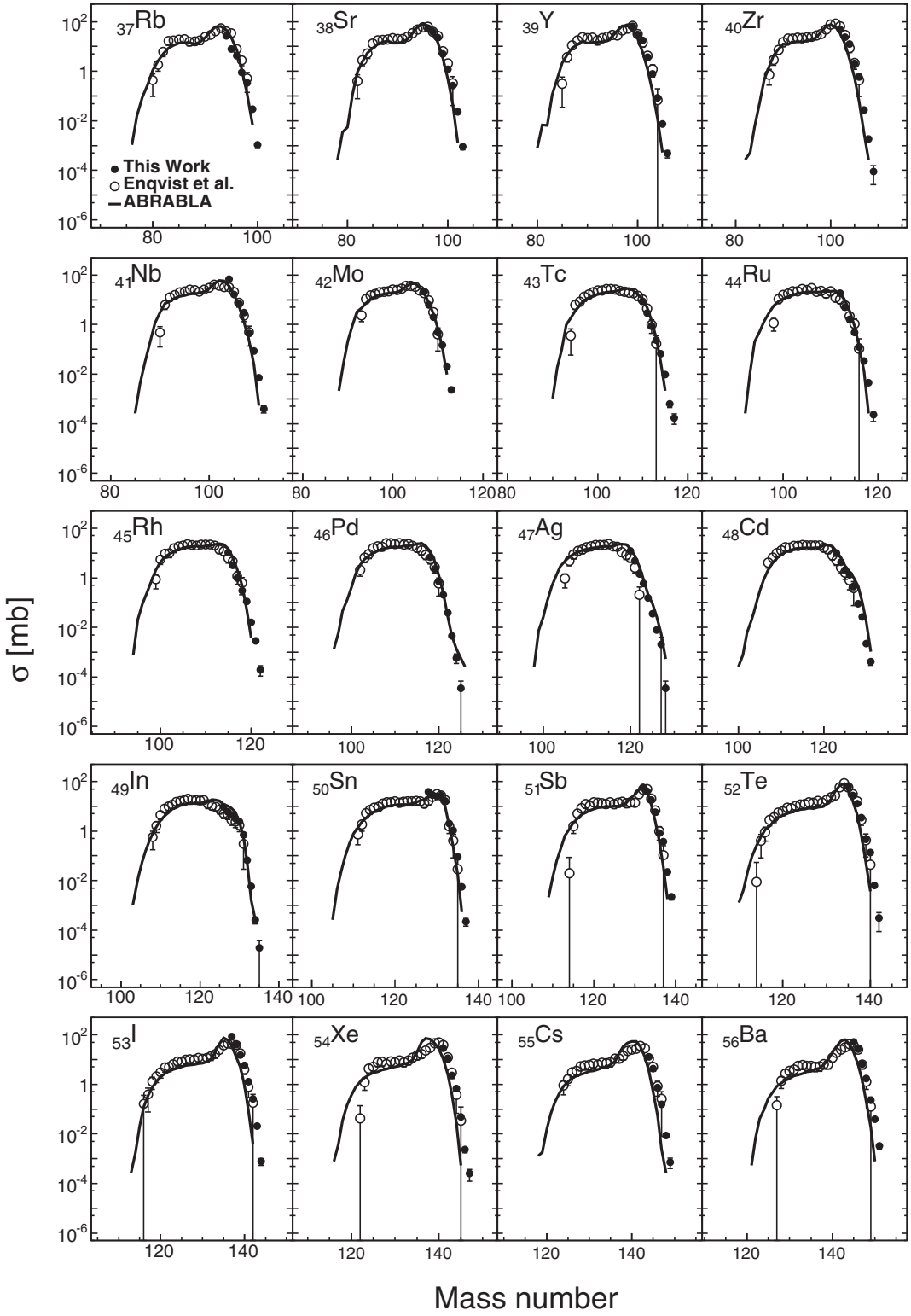

FIG. 4. Isotopic distributions of the production cross sections of the fission fragments investigated in this work with a lead target (filled circles) compared with the fragments measured previously by Enqvist and collaborators [22] for the same reaction (open circles) and predictions obtained with the code ABRABLA07 (solid line).

observation clearly demonstrates the dominance of electromagnetic-induced fission when using a lead target in the energy regime used for investigating this reaction. Therefore, we expect that the main features of the measured production yields will be determined by fission processes at excitation energies between 10 and 15 MeV defined mostly by

the excitation of the giant-dipole resonance in ^{238}U. Similar conclusions were obtained by Donzaud and collaborators [24] investigating the same reaction but at a slightly lower projectile energy, 750*A* MeV.

Figure 4 also shows predicted cross sections of the fission fragments produced in this reaction using the code ABRABLA07 (solid line) [25,26]. This code describes the properties of the projectile spectators issued in peripheral and semiperipheral collisions of heavy ions at relativistic energies. The code is based on the abrasion ablation model but also includes Coulomb excitation [14], and a statistical description of the fission process with a realistic model of the fission yields [27,28]. As can be seen, ABRABLA07 provides a rather good overall description of the data. A detailed comparison reveals that the yields of the most neutron-rich nuclei produced in asymmetric splittings are slightly underestimated, while the more neutron-deficient ones are rather well described. The production of nuclei in symmetric splittings is well described for the complete isotopic chains.

C. Fission induced by the beryllium target

In Fig. 5 we report the isotopic production cross sections of the most neutron-rich medium-mass nuclei measured in this work with the beryllium target (filled squares). The most neutron-rich nuclei produced in ^{238}U on beryllium reactions have recently been measured [10]. However, these measurements were done at a rather different energy, 345*A* MeV, and the obtained isotopic distributions do not cover the maximum of the fission yields. Isotopic distributions of fission fragments across the maximum production yield have only been obtained for the reaction $^{238}\mathrm{U} + d$ at 1000*A* MeV, again using the FRS and a detection setup similar to the one used in this work, by Pereira *et al.* [17] (open squares). In principle, with the exception of the difference in total reaction cross section (≈53%), one expects that the production of fission fragments in both reactions should be similar since the difference in atomic number between the two targets is small and we expect a negligible effect of Coulomb excitation. Therefore, fission should be mostly induced by nuclear interaction in both targets. Indeed, the comparison of both sets of data presented in Fig. 5 shows a good overlap and complementarity. As in the measurements with the lead target, the present data cover the production of the most neutron-rich fission residues, with the lowest cross sections, while the previous measurement provides a complete scan of the production of medium-mass residual fragments produced in fission reactions, although for a limited range of cross sections.

As shown in Fig. 5, the yields of the more neutron-rich fragments measured with the beryllium and deuterium target, produced in fission reactions, present a different pattern with respect to those obtained with the lead target. The production of heavy fragments around the spherical shell at $N \approx 82$ (^{134}Te and ^{142}Xe) and the deformed one at $N \approx 88$, and their complementary fragments (^{104}Zr and ^{96}Sr), is very much reduced compared to the productions of the same nuclei with the lead target. In fact, the beryllium/deuterium data indicate that those fragments were most likely produced in reactions where fission occurs on average for excitation energies well above 20 MeV.

Figure 5 also represents by the solid line the predictions obtained with the code ABRABLA07 for the reaction $^{238}\mathrm{U}$ + Be at 1000*A* MeV. As for the lead target, the code provides a rather good agreement with the most neutron-rich fission fragments measured in this work. Fission fragments with a moderate neutron excess measured in the reaction $^{238}\mathrm{U} + d$ at 1000*A* MeV are also rather well described. However, one can again observe a small underestimation of the production of the most neutron-rich nuclei for the asymmetric splittings, which would indicate that the measured mass distributions are slightly broader than the calculated ones.

IV. TARGET DEPENDENCE OF THE FISSION YIELDS

A. Target thickness

The final yields of residual nuclei produced by in-flight projectile fission depends not only on the reaction mechanism, but also on the target nature and thickness. The production of a given fragment increases with the thickness of the target. However, secondary reactions increasing also with the target thickness may contribute to the production and destruction of the same fragment. An example is the production of very neutron-rich fragments in the secondary fragmentation reactions of fission fragments [13]. Another important effect will be the increase with the target thickness of the energy and location straggling, limiting the transmission through the magnetic spectrometer. Therefore, an optimum target thickness exists which maximizes the production yields. In the particular case of the setup used in the present work, this optimum production is reached for a target thickness between 10% and 20% of the range of the incoming projectiles [29].

For a typical 1000*A* MeV ^{238}U beam used to induce in-flight fission, the optimum target thicknesses corresponding to 20% of the range of this projectiles in beryllium and lead would be 2060 and 3135 mg/cm^2, respectively. For the final production one should also consider that the lower mass number of beryllium leads to 23 more atoms per unit area compared to lead, which largely compensates for the 30% thicker targets one can use with lead. Therefore, assuming the same production cross section, a beryllium target should produce up to a factor of 10 more fragments than a lead target.

B. Target nuclei

The composition of the target will also affect the reaction mechanism and probability. Not only will heavy targets increase the total reaction cross section due to nuclear interactions (fragmentation reactions) but also, as discussed in the previous section, the larger atomic number will favor electromagnetic excitations. These excitations induce low-energy fission with rather large cross sections, leading to an asymmetric fission fragment distribution. In light targets one mostly expects nuclear-induced fission at higher excitation energies with a symmetric fission fragment distribution.

To display how the different reaction mechanisms, favored by these two targets, affect the production yields obtained

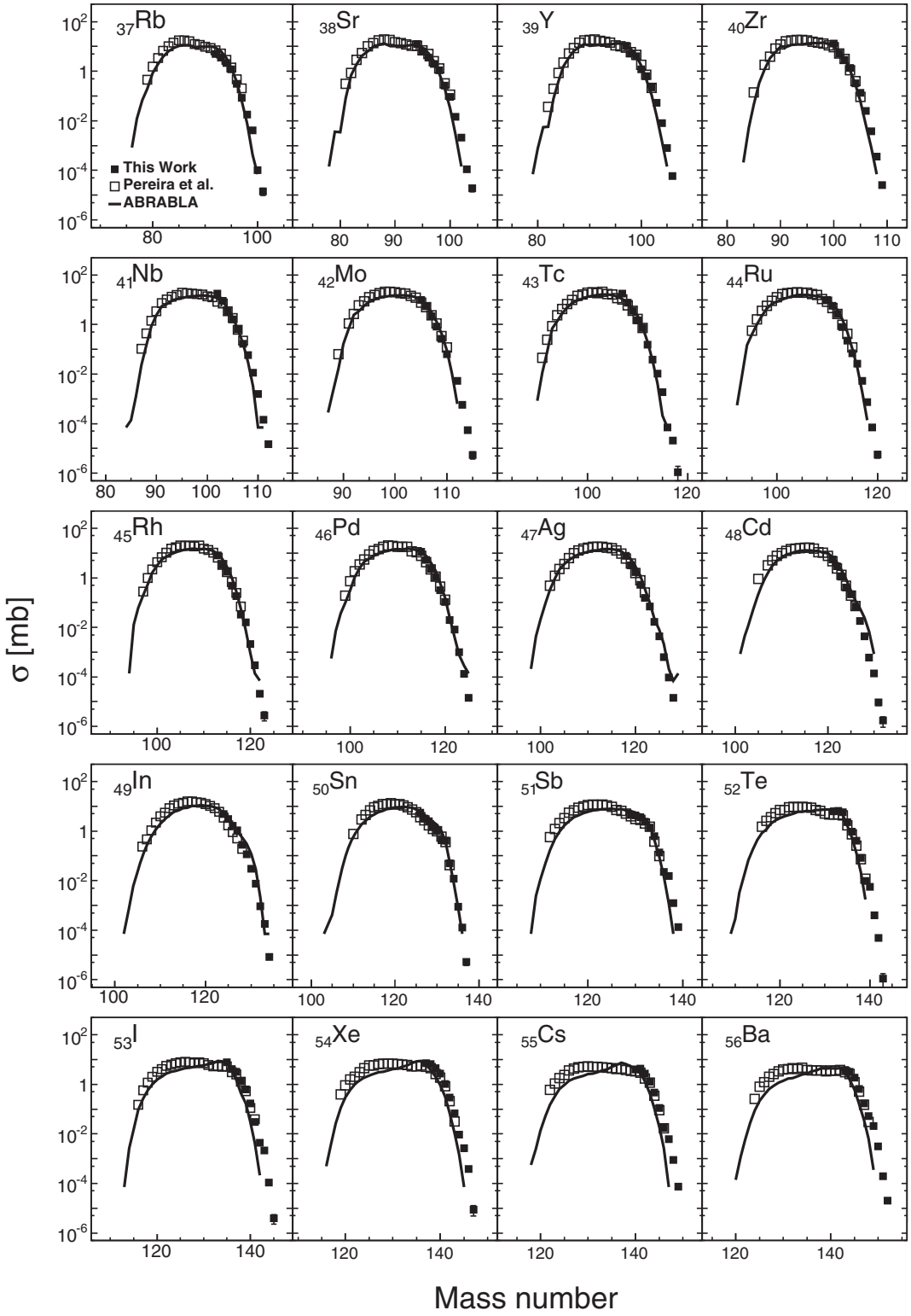

FIG. 5. Isotopic distributions of the production cross sections of the fission fragments investigated in this work with a beryllium target (filled squares) compared with the fragments measured previously by Pereira and collaborators [17] for the reaction ^{238}U + d at 1000A MeV (open squares) and predictions obtained with the code ABRABLA07 for the reaction ^{238}U + Be at 1000A MeV (solid line).

in projectile in-flight fission of ^{238}U, in Fig. 6 we compare the yields that one would expect from the two sets of data obtained in this work, but using targets with the optimum thicknesses discussed above. In the present experiment thinner targets were used in order to optimize the transmission of ^{132}Sn for another purpose. The comparison of the sets of data

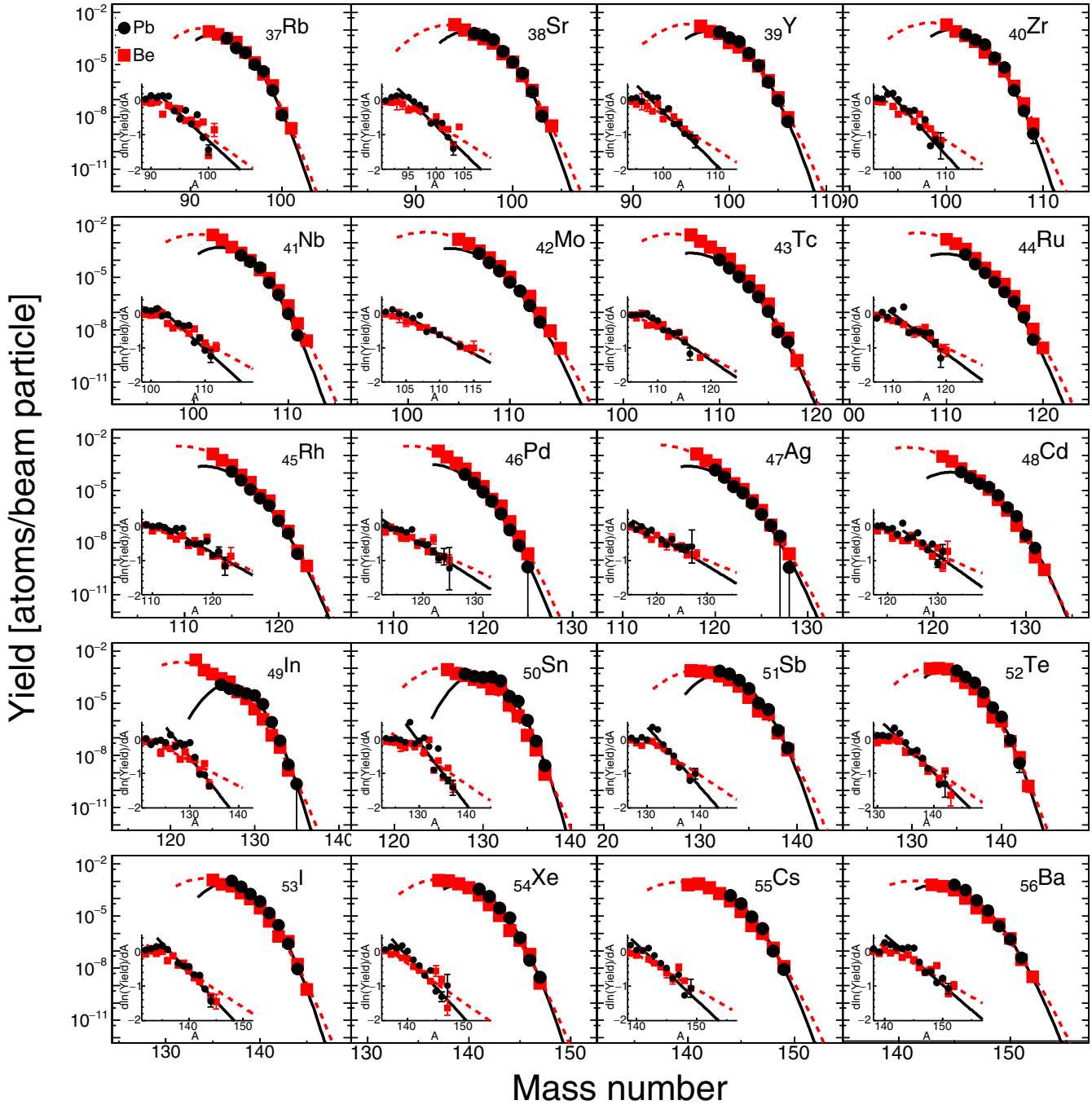

FIG. 6. Production yields per beam particle of the fragments obtained in the fission of ^{238}U on beryllium (red squares) and lead (black circles) targets at 950*A* MeV, assuming 20% of the range of the projectiles as the target thickness. Insets: Evolution of the local derivatives of the logarithm of the measured yields according to the neutron excess. Dashed and solid lines represent fits of the beryllium and lead data, respectively.

presented in Fig. 6 shows some clear differences in the yields obtained with the two targets.

The more symmetric splittings, from molybdenum to silver, show a clear enhancement of the production yields with the beryllium target for all fission fragments. Moreover, this enhancement factor seems to be rather similar for all nuclei. This result would indicate that the same reaction mechanism dominates in the formation of symmetric fission fragments in both targets, and the difference in the final yields is mostly governed by the differences in total fission cross section and the number of atoms per unit area in the target. Indeed, in the previous section it was already discussed that symmetric splittings of ^{238}U are favored by high excitation energies such as the ones reached in fragmentation reactions. Therefore, for

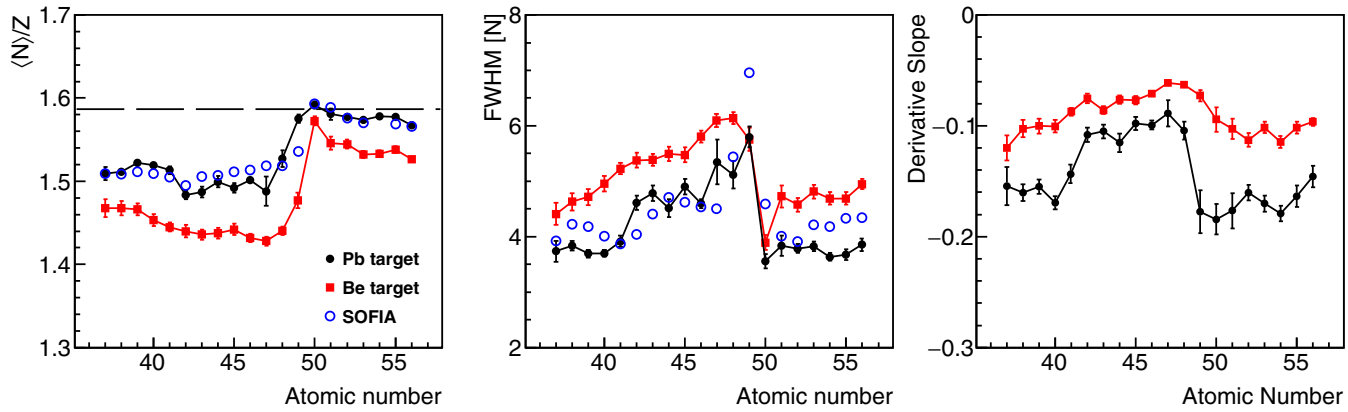

FIG. 7. Mean value of the neutron-to-proton ratio (left panel), the full width at half-maximum (center panel), and the slope of the distributions (right panel) obtained from the fit of the isotopic yields presented in Fig. 6 as a function of the atomic number of the fission fragments. Open symbols correspond to data obtained for the reaction ^{238}U on lead at 650A MeV.

the observed residual nuclei produced in symmetric fission the fragmentation-fission process is in both targets most likely the dominant reaction mechanism.

One observes, however, a difference between the two targets for the asymmetric splittings. The production of nuclei around the shell closures ($N = 82$–86, $Z = 50$) is clearly enhanced with the lead target. This effect is particularly visible in heavy fission fragments, from indium to barium, with neutron numbers between 80 and 86. However, for the most neutron-rich isotopes of these elements the production yields appear to be rather similar or even slightly larger with the beryllium target. In this case, one understands the larger production of some isotopes with the lead target as a consequence of the Coulomb excitations leading to low-energy fission enhancing asymmetric splittings governed by the shell closures. The similar yields observed for the most neutron-rich isotopes of these elements would indicate that the dominant mechanism for the production of these fragments is no longer low-energy fission but fission at higher excitation energies induced by nuclear interactions (fragmentation) in both targets. In this case the larger number of atoms per unit area in the beryllium target would even compensate for the larger total nuclear reaction cross section and the optimum thickness of the lead target.

For light fission fragments, from rubidium to niobium, the yield enhancement due to low-energy fission induced by the lead target is very much reduced. Moreover, the production of the most neutron-rich nuclei appears to be larger with the beryllium target. This relative increase in the yields obtained with the beryllium target can be explained by fission of compound nuclei lighter than ^{238}U, such as the ones produced in fragmentation reactions, but also by the larger number of atoms per unit area in the beryllium target.

C. Yield parametrization from fits

The qualitative conclusions discussed in the previous paragraphs can be quantified by fitting the yields to systematically investigate the evolution of the mean neutron excess and width of the isotopic distributions. Moreover, the fits can be used to extrapolate the yields towards larger values of neutron excess. We have fitted the most neutron-rich part of the measured yield distributions from its maximum to a parabolic function in logarithmic scale. In these fits we have used the additional data shown in Figs. 4 and 5. The dashed line in Fig. 6 represents the results of the fits of the data obtained with the beryllium target, while the solid line corresponds to the fits of the lead data.

The fits indicate that for isotopic distributions of fragments around $Z = 46$, corresponding to symmetric fission events, the slopes describing the evolution of the yields with the neutron excess are rather similar for both targets. However, for heavier and lighter fission fragments, mostly produced in asymmetric fission events, the slopes are steeper with the lead target. This behavior can also be shown by plotting the evolution of the local derivatives of the logarithm of the measured yields according to the neutron excess, as shown in the insets in Fig. 6. The slope of the yield distributions is obtained by linear fits of these local derivatives as a function of the neutron excess.

The global trends of the isotopic distributions of the fission yields can be analyzed by plotting the evolution of the parameters of the fits characterizing these isotopic distributions as a function of the atomic element of the residual fragment. In Fig. 7 we represent the evolution of the mean N/Z value of the distributions (left panel), the width of the distributions at half-maximum (center panel), and the slope of the production yields of the most neutron-rich residual nuclei (right panel). For completion, we also report the results obtained from fits of the isotopic distributions of fission residues obtained in a similar reaction, ^{238}U + Pb at 650A MeV, but measured with the R3B/SOFIA experimental setup [30].

In the left panel, the dashed line corresponds to the expected N/Z value assuming the conservation of the neutron-to-proton ratio of ^{238}U in the fission process. The evolution of the mean N/Z value of these distributions shows that fragments produced in fission reactions induced by the lead target have on average a larger neutron excess than those produced with the beryllium target, as previously concluded from the analysis in Fig. 6. The central panel in Fig. 7 clearly indicates that the average width of the distributions of the most neutron-rich fission residues is larger with the beryllium target

than with the lead one. In both cases one also observes a clear dependence of the width as a function of the asymmetry of the splitting. Symmetric partitions present broader isotopic distributions than asymmetric ones. The good agreement between the data obtained in this work with the lead target and the results of the R3B/SOFIA experiment confirms the validity of the present analysis despite the fact that we only measured the most neutron-rich part of the isotopic distributions of the fission fragments.

The lower mean values of N/Z and the larger values of the width of the distributions obtained with the beryllium target compared to those with lead can be understood in terms of the lighter fissioning systems produced in fragmentation reactions induced by the beryllium target and by the higher excitation energies reached in this case. The width and average N/Z value of these distributions also show a drastic change in their evolution at the closed shell $Z = 50$. This is the well-known charge polarization in fission induced by shell effects [31,32].

The evolution of the slopes of the production yields presented in the right panel in Fig. 7 shows that the isotopic distributions produced in symmetric splits are not very different for the two targets, while for the asymmetric fissions the slopes obtained with the lead target are clearly steeper than the ones corresponding to the beryllium target. The steeper slopes observed with lead for asymmetric fission are most likely caused by the strong and local enhancement of the yields of fission fragments with neutron numbers between 80 and 86, induced by the large cross section of low-energy fissions in Coulomb excitation reactions. For larger values of the neutron excess, fission fragments are then expected to be produced by nuclear interactions. Therefore, it does not seem reasonable to use these slopes, mixing both reaction mechanisms, to extrapolate the production yields.

The situation is rather different for the beryllium target because the production of fission fragments is mostly governed by a single reaction mechanism, fragmentation-induced fission. In this case, the fits could be used to extrapolate the production yields for extremely neutron-rich fission fragments. Such an extrapolation would be based on the assumption that fluctuations in the neutron excess of the final fission fragments are purely statistical and they scale with temperature [33,34], however, we cannot exclude that the maximum neutron excess could be limited by quantum-mechanical zero-point oscillations [35,36].

The results of these fits are in good agreement with the evolution and magnitude of the same parameters obtained in the characterization of the low-energy component in fission reactions induced by relativistic ^{238}U projectiles impinging on protons [37], deuterons [15], and lead [24]. The slight differences observed for the width of the more symmetric partitions, and in general with the beryllium target, are due to the different functions used for the fit. In the previous works two Gaussian functions were used to characterize the low- and high-energy components in fission. In the present work we use a single function in order to improve the description of the production yields of the most neutron-rich isotopes and, thus, obtain more reliable extrapolations.

From this analysis we can conclude that the smaller value of the average N/Z and the larger width in the distributions measured with the beryllium target are due to the high-energy fission component. According to the extrapolated yields from the fits, this high-energy component would be responsible for the production of the most neutron-rich nuclei in the fission of ^{238}U. Therefore it seems that fragmentation-induced fission using light targets such as beryllium, present clear advantages for the production of medium-mass neutron-rich nuclei. On top of the larger number of scattering centers per surface unit in the target, fission induced at relatively high excitation energies enhances fluctuations in mass asymmetry and neutron excess. In this way we increase not only the range of atomic number of the final residual nuclei but also their neutron excess. Nevertheless, the use of high-Z targets, such as lead, can be of interest to enhance the production of fission fragments around the double-shell closure ($N \approx 82$–86, $Z \approx 50$) and its complementary light fragments.

V. CONCLUSIONS

In the present work, we have investigated the role of the target in the production of medium-mass neutron-rich nuclei by in-flight fission of ^{238}U. For this purpose, an experiment was performed at GSI to measure the production cross sections of neutron-rich fragments in fission reactions of ^{238}U using the inverse kinematics technique. The beam, accelerated to 950A MeV, impinged upon two targets, lead and beryllium, enhancing low- and high-energy fission, respectively. Using the high-resolution magnetic spectrometer FRS, the yield distributions of unambiguously identified fission fragments were investigated. We have measured production cross sections of neutron-rich nuclei from $Z = 36$ to $Z = 60$ down to 100 pb for both targets. The experimental data were extrapolated in order to find out which target could produce the most neutron-rich nuclei.

The data show that the mass distribution of fission fragments obtained with the lead target is asymmetric, while the distribution becomes symmetric with the beryllium target. These different shapes are understood as a consequence of the different reaction mechanisms inducing fission in both targets. In low-Z targets such as beryllium, fragmentation-induced fission is responsible for the production of medium-mass neutron-rich nuclei in reactions induced by ^{238}U at relativistic energies. In contrast, in higher-Z targets, like lead, fission can also be induced by Coulomb excitations. The difference in excitation energy of the fissioning nuclei produced by these two reaction mechanisms would explain the final shapes of the yield distributions. Coulomb excitation induces low-energy fission where the splitting of the fission fragments is governed by shell effects in the final fragments. Therefore this mechanism enhances the production of fission fragments around the shell closures ($N \approx 82$–86, $Z \approx 50$). Fragmentation produces fissioning nuclei with much higher excitation energies on average. Under those conditions shell effects disappear and the final distributions become symmetric. Moreover, statistical fluctuations seem to be responsible for the broadening of the mass asymmetry and neutron excess distributions. However, the contribution of secondary reactions in thick targets to the production of the most neutron-rich fragments should not be neglected.

The comparison of the two sets of data measured in this work confirms that, with the exception of the $N \approx 80$–86, $Z \approx 48$–52 region, the production yields with the beryllium target are clearly favored by the larger number of scattering centers per unit area, compared to higher-Z targets.

ACKNOWLEDGMENTS

This work was partially funded by the EC under EURISOL-DS Contract No. 515768 RIDS, by the Spanish Ministry of Education and Science under Grant No. FPA2010-22174-C02-01(02), and by Xunta de Galicia under Grant No. GRC ED431C 2017/54.

APPENDIX: MEASURED PRODUCTION CROSS SECTIONS

Tables I and II list the isotopic production cross sections in ^{238}U fission induced by lead and beryllium targets, respectively.

TABLE I. Isotopic production cross sections measured with the Pb target.

Isotope	Cross section (mb)	Isotope	Cross section (mb)	Isotope	Cross section (mb)	Isotope	Cross section (mb)
^{90}Kr	50 ± 20	^{111}Mo	$(1.5 \pm 0.5) \times 10^{-1}$	^{124}Cd	4 ± 1	^{138}I	40 ± 10
^{91}Kr	3 ± 1	^{112}Mo	$(2.0 \pm 0.7) \times 10^{-2}$	^{125}Cd	2.1 ± 0.6	^{139}I	15 ± 5
^{94}Rb	30 ± 9	^{113}Mo	$(2.3 \pm 0.8) \times 10^{-3}$	^{126}Cd	1.3 ± 0.4	^{140}I	6 ± 2
^{95}Rb	8 ± 2	^{110}Tc	9 ± 3	^{127}Cd	$(4 \pm 1) \times 10^{-1}$	^{141}I	1.2 ± 0.4
^{96}Rb	4 ± 1	^{111}Tc	3.0 ± 0.9	^{128}Cd	$(9 \pm 3) \times 10^{-2}$	^{142}I	$(2.5 \pm 0.8) \times 10^{-1}$
^{97}Rb	$(9 \pm 3) \times 10^{-1}$	^{112}Tc	$(9 \pm 3) \times 10^{-1}$	^{129}Cd	$(2.7 \pm 0.9) \times 10^{-2}$	^{143}I	$(2.1 \pm 0.7) \times 10^{-2}$
^{98}Rb	$(3 \pm 1) \times 10^{-1}$	^{113}Tc	$(2.4 \pm 0.8) \times 10^{-1}$	^{130}Cd	$(2.2 \pm 0.8) \times 10^{-3}$	^{144}I	$(8 \pm 3) \times 10^{-4}$
^{99}Rb	$(3.0 \pm 0.9) \times 10^{-2}$	^{114}Tc	$(6 \pm 2) \times 10^{-2}$	^{131}Cd	$(4 \pm 2) \times 10^{-4}$	^{141}Xe	28 ± 9
^{100}Rb	$(1.1 \pm 0.4) \times 10^{-3}$	^{115}Tc	$(9 \pm 3) \times 10^{-3}$	^{126}In	10 ± 3	^{142}Xe	11 ± 4
^{96}Sr	50 ± 20	^{116}Tc	$(6 \pm 3) \times 10^{-4}$	^{127}In	6 ± 2	^{143}Xe	2.3 ± 0.7
^{97}Sr	40 ± 10	^{117}Tc	$(1.7 \pm 0.9) \times 10^{-4}$	^{128}In	4 ± 1	^{144}Xe	$(7 \pm 2) \times 10^{-1}$
^{98}Sr	23 ± 7	^{112}Ru	19 ± 6	^{129}In	3 ± 1	^{145}Xe	$(5 \pm 2) \times 10^{-2}$
^{99}Sr	5 ± 2	^{113}Ru	5 ± 2	^{130}In	2.4 ± 0.8	^{146}Xe	$(2.4 \pm 1) \times 10^{-3}$
^{100}Sr	1.2 ± 0.4	^{114}Ru	1.6 ± 0.5	^{131}In	$(7 \pm 2) \times 10^{-1}$	^{147}Xe	$(2 \pm 1) \times 10^{-4}$
^{101}Sr	$(2.7 \pm 0.8) \times 10^{-1}$	^{115}Ru	$(5 \pm 2) \times 10^{-2}$	^{132}In	$(7 \pm 2) \times 10^{-2}$	^{144}Cs	13 ± 4
^{102}Sr	$(2.3 \pm 0.8) \times 10^{-2}$	^{116}Ru	$(1.2 \pm 0.4) \times 10^{-1}$	^{133}In	$(6 \pm 2) \times 10^{-3}$	^{145}Cs	4 ± 1
^{103}Sr	$(9 \pm 4) \times 10^{-4}$	^{117}Ru	$(3 \pm 1) \times 10^{-2}$	^{134}In	$(3 \pm 1) \times 10^{-4}$	^{146}Cs	$(7 \pm 2) \times 10^{-1}$
^{99}Y	60 ± 20	^{118}Ru	$(4 \pm 2) \times 10^{-3}$	^{135}In	$(2 \pm 2) \times 10^{-5}$	^{147}Cs	$(1.6 \pm 0.5) \times 10^{-1}$
^{100}Y	30 ± 10	^{119}Ru	$(2 \pm 1) \times 10^{-4}$	^{128}Sn	39 ± 12	^{148}Cs	$(8 \pm 3) \times 10^{-3}$
^{101}Y	18 ± 6	^{115}Rh	10 ± 3	^{129}Sn	29 ± 9	^{149}Cs	$(7 \pm 4) \times 10^{-4}$
^{102}Y	3 ± 1	^{116}Rh	3 ± 1	^{130}Sn	25 ± 8	^{145}Ba	50 ± 20
^{103}Y	$(8 \pm 2) \times 10^{-1}$	^{117}Rh	1.0 ± 0.3	^{131}Sn	27 ± 9	^{146}Ba	26 ± 8
^{104}Y	$(8 \pm 3) \times 10^{-2}$	^{118}Rh	$(3 \pm 1) \times 10^{-1}$	^{132}Sn	16 ± 5	^{147}Ba	6 ± 2
^{105}Y	$(8 \pm 2) \times 10^{-3}$	^{119}Rh	$(1.1 \pm 0.5) \times 10^{-1}$	^{133}Sn	2.0 ± 0.6	^{148}Ba	1.7 ± 0.6
^{106}Y	$(5 \pm 2) \times 10^{-4}$	^{120}Rh	$(1.6 \pm 0.5) \times 10^{-2}$	^{134}Sn	1.1 ± 0.3	^{149}Ba	$(2.2 \pm 0.7) \times 10^{-1}$
^{102}Zr	50 ± 20	^{121}Rh	$(3 \pm 1) \times 10^{-3}$	^{135}Sn	$(9 \pm 3) \times 10^{-2}$	^{150}Ba	$(4 \pm 1) \times 10^{-2}$
^{103}Zr	24 ± 8	^{122}Rh	$(2 \pm 1) \times 10^{-4}$	^{136}Sn	$(6 \pm 2) \times 10^{-3}$	^{151}Ba	$(3 \pm 1) \times 10^{-3}$
^{104}Zr	12 ± 4	^{118}Pd	7 ± 2	^{137}Sn	$(2 \pm 1) \times 10^{-4}$	^{148}La	19 ± 6
^{105}Zr	2.1 ± 0.7	^{119}Pd	2.2 ± 0.7	^{132}Sb	60 ± 20	^{149}La	8 ± 2
^{106}Zr	$(6 \pm 2) \times 10^{-1}$	^{120}Pd	$(7 \pm 2) \times 10^{-1}$	^{133}Sb	40 ± 10	^{150}La	1.3 ± 0.4
^{107}Zr	$(2.8 \pm 0.9) \times 10^{-2}$	^{121}Pd	$(2.1 \pm 0.7) \times 10^{-1}$	^{134}Sb	18 ± 6	^{151}La	$(1.7 \pm 0.6) \times 10^{-1}$
^{108}Zr	$(1.9 \pm 0.7) \times 10^{-3}$	^{122}Pd	$(3 \pm 1) \times 10^{-2}$	^{135}Sb	6 ± 2	^{152}La	$(2.6 \pm 0.9) \times 10^{-2}$
^{109}Zr	$(9 \pm 7) \times 10^{-5}$	^{123}Pd	$(4 \pm 2) \times 10^{-3}$	^{136}Sb	$(8 \pm 3) \times 10^{-1}$	^{153}La	$(3 \pm 1) \times 10^{-3}$
^{104}Nb	70 ± 20	^{124}Pd	$(6 \pm 3) \times 10^{-4}$	^{137}Sb	$(4 \pm 1) \times 10^{-1}$	^{151}Ce	6 ± 2
^{105}Nb	16 ± 5	^{125}Pd	$(3 \pm 3) \times 10^{-5}$	^{138}Sb	$(2.3 \pm 0.8) \times 10^{-2}$	^{152}Ce	$(1.6 \pm 0.5$
^{106}Nb	7 ± 2	^{120}Ag	12 ± 4	^{139}Sb	$(2.2 \pm 0.9) \times 10^{-3}$	^{153}Ce	$(1.9 \pm 0.6) \times 10^{-1}$
^{107}Nb	3 ± 1	^{121}Ag	5 ± 2	^{135}Te	60 ± 20	^{154}Ce	$(3 \pm 1) \times 10^{-2}$
^{108}Nb	$(4 \pm 1) \times 10^{-1}$	^{122}Ag	1.4 ± 0.4	^{136}Te	27 ± 8	^{152}Pr	14 ± 4
^{109}Nb	$(8 \pm 3) \times 10^{-2}$	^{123}Ag	$(6 \pm 2) \times 10^{-1}$	^{137}Te	13 ± 4	^{153}Pr	4 ± 1
^{110}Nb	$(7 \pm 2) \times 10^{-3}$	^{124}Ag	$(1.6 \pm 0.5) \times 10^{-1}$	^{138}Te	3 ± 1	^{155}Pr	$(1.8 \pm 0.6) \times 10^{-1}$
^{111}Nb	$(4 \pm 2) \times 10^{-4}$	^{125}Ag	$(4 \pm 1) \times 10^{-2}$	^{139}Te	$(5 \pm 2) \times 10^{-1}$	^{155}Nd	4 ± 1
^{107}Mo	21 ± 7	^{126}Ag	$(8 \pm 3) \times 10^{-3}$	^{140}Te	$(1.3 \pm 0.4) \times 10^{-1}$	^{156}Nd	0.9 ± 0.3
^{108}Mo	6 ± 2	^{127}Ag	$(2 \pm 2) \times 10^{-3}$	^{141}Te	$(6 \pm 2) \times 10^{-3}$		
^{109}Mo	$(2.0 \pm 0.6$	^{128}Ag	$(3 \pm 3) \times 10^{-5}$	^{142}Te	$(3 \pm 2) \times 10^{-4}$		
^{110}Mo	$(5 \pm 2) \times 10^{-1}$	^{123}Cd	10 ± 3	^{137}I	80 ± 30		

TABLE II. Isotopic production cross sections measured with the Be target.

Isotope	Cross section (mb)	Isotope	Cross section (mb)	Isotope	Cross section (mb)	Isotope	Cross section (mb)
^{80}Ga	$(4 \pm 1) \times 10^{-3}$	^{99}Zr	50 ± 20	^{117}Pd	2.3 ± 0.7	^{133}Te	7 ± 2
^{84}Ga	$(5 \pm 3) \times 10^{-5}$	^{100}Zr	13 ± 4	^{118}Pd	1.1 ± 0.4	^{134}Te	6 ± 2
^{79}Ge	$(4 \pm 4) \times 10^{-1}$	^{101}Zr	5 ± 2	^{119}Pd	$(3 \pm 1) \times 10^{-1}$	^{135}Te	2.3 ± 0.7
^{80}Ge	$(1 \pm 1) \times 10^{-1}$	^{102}Zr	2.9 ± 0.9	^{120}Pd	$(1.1 \pm 0.3) \times 10^{-1}$	^{136}Te	0.9 ± 0.3
^{82}Ge	$(6 \pm 2) \times 10^{-2}$	^{103}Zr	1.4 ± 0.4	^{121}Pd	$(1.9 \pm 0.7) \times 10^{-2}$	^{137}Te	$(4 \pm 1) \times 10^{-1}$
^{83}Ge	$(6 \pm 3) \times 10^{-3}$	^{104}Zr	$(3 \pm 1) \times 10^{-1}$	^{122}Pd	$(8 \pm 3) \times 10^{-3}$	^{138}Te	$(8 \pm 3) \times 10^{-2}$
^{84}Ge	$(5 \pm 2) \times 10^{-4}$	^{105}Zr	$(1.3 \pm 0.4) \times 10^{-1}$	^{123}Pd	$(1.0 \pm 0.3) \times 10^{-3}$	^{139}Te	$(9 \pm 3) \times 10^{-3}$
^{81}As	1 ± 1	^{106}Zr	$(2.5 \pm 0.8) \times 10^{-2}$	^{124}Pd	$(1.3 \pm 0.4) \times 10^{-4}$	^{140}Te	$(6 \pm 2) \times 10^{-3}$
^{82}As	$(3 \pm 2) \times 10^{-1}$	^{107}Zr	$(4 \pm 1) \times 10^{-3}$	^{125}Pd	$(1.4 \pm 0.5) \times 10^{-5}$	^{141}Te	$(4 \pm 1) \times 10^{-4}$
^{83}As	$(2 \pm 2) \times 10^{-1}$	^{108}Zr	$(4 \pm 1) \times 10^{-4}$	^{118}Ag	8 ± 3	^{142}Te	$(5 \pm 2) \times 10^{-5}$
^{85}As	$(4 \pm 1) \times 10^{-2}$	^{109}Zr	$(2.5 \pm 0.9) \times 10^{-5}$	^{119}Ag	3 ± 1	^{143}Te	$(1.1 \pm 0.7) \times 10^{-6}$
^{86}As	$(4 \pm 1) \times 10^{-3}$	^{102}Nb	18 ± 6	^{120}Ag	1.7 ± 0.6	^{135}I	8 ± 2
^{87}As	$(8 \pm 3) \times 10^{-4}$	^{103}Nb	9 ± 3	^{121}Ag	$(5 \pm 2) \times 10^{-1}$	^{136}I	4 ± 1
^{88}As	$(1.5 \pm 0.5) \times 10^{-4}$	^{104}Nb	3 ± 1	^{122}Ag	$(1.5 \pm 0.6) \times 10^{-1}$	^{137}I	3 ± 1
^{84}Se	1.1 ± 0.6	^{105}Nb	1.6 ± 0.5	^{123}Ag	$(7 \pm 2) \times 10^{-2}$	^{138}I	1.3 ± 0.4
^{85}Se	$(3 \pm 2) \times 10^{-1}$	^{106}Nb	$(6 \pm 2) \times 10^{-1}$	^{124}Ag	$(1.6 \pm 0.6) \times 10^{-2}$	^{139}I	$(6 \pm 2) \times 10^{-1}$
^{87}Se	5 ± 2	^{107}Nb	$(1.7 \pm 0.5) \times 10^{-1}$	^{125}Ag	$(4 \pm 1) \times 10^{-3}$	^{140}I	$(1.7 \pm 0.6) \times 10^{-1}$
^{88}Se	$(2.4 \pm 0.8) \times 10^{-2}$	^{108}Nb	$(6 \pm 2) \times 10^{-2}$	^{126}Ag	$(6 \pm 2) \times 10^{-4}$	^{141}I	$(3 \pm 1) \times 10^{-2}$
^{89}Se	$(3 \pm 1) \times 10^{-3}$	^{109}Nb	$(1.2 \pm 0.4) \times 10^{-2}$	^{127}Ag	$(1.0 \pm 0.3) \times 10^{-4}$	^{142}I	$(4 \pm 2) \times 10^{-3}$
^{90}Se	$(4 \pm 2) \times 10^{-4}$	^{110}Nb	$(1.6 \pm 0.5) \times 10^{-3}$	^{128}Ag	$(1.4 \pm 0.5) \times 10^{-5}$	^{143}I	$(2.2 \pm 0.7) \times 10^{-3}$
^{86}Br	11 ± 5	^{111}Nb	$(1.4 \pm 0.5) \times 10^{-4}$	^{121}Cd	6 ± 2	^{144}I	$(1.1 \pm 0.4) \times 10^{-4}$
^{87}Br	1.2 ± 0.5	^{112}Nb	$(1.5 \pm 0.6) \times 10^{-5}$	^{122}Cd	2.9 ± 0.9	^{145}I	$(4 \pm 2) \times 10^{-6}$
^{88}Br	$(5 \pm 2) \times 10^{-1}$	^{105}Mo	10 ± 3	^{123}Cd	1.1 ± 0.4	^{137}Xe	7 ± 2
^{89}Br	$(2 \pm 1) \times 10^{-1}$	^{106}Mo	6 ± 2	^{124}Cd	$(4 \pm 1) \times 10^{-1}$	^{138}Xe	7 ± 2
^{91}Br	$(6 \pm 2) \times 10^{-3}$	^{107}Mo	2.2 ± 0.7	^{125}Cd	$(2.2 \pm 0.7) \times 10^{-1}$	^{139}Xe	4 ± 1
^{92}Br	$(1.9 \pm 0.6) \times 10^{-2}$	^{108}Mo	$(8 \pm 3) \times 10^{-1}$	^{126}Cd	$(7 \pm 2) \times 10^{-2}$	^{140}Xe	2.7 ± 0.9
^{93}Br	$(1.5 \pm 0.5) \times 10^{-2}$	^{109}Mo	$(2.7 \pm 0.9) \times 10^{-1}$	^{127}Cd	$(1.8 \pm 0.6) \times 10^{-2}$	^{141}Xe	1.0 ± 0.3
^{94}Br	$(5 \pm 2) \times 10^{-3}$	^{110}Mo	$(6 \pm 2) \times 10^{-2}$	^{128}Cd	$(4 \pm 1) \times 10^{-3}$	^{142}Xe	$(3 \pm 1) \times 10^{-1}$
^{89}Kr	3 ± 1	^{112}Mo	$(5 \pm 2) \times 10^{-3}$	^{129}Cd	$(6 \pm 2) \times 10^{-4}$	^{143}Xe	$(7 \pm 2) \times 10^{-2}$
^{90}Kr	2.5 ± 0.9	^{113}Mo	$(6 \pm 2) \times 10^{-4}$	^{130}Cd	$(1.4 \pm 0.5) \times 10^{-4}$	^{144}Xe	$(9 \pm 3) \times 10^{-3}$
^{91}Kr	2.9 ± 0.9	^{114}Mo	$(6 \pm 2) \times 10^{-5}$	^{131}Cd	$(9 \pm 4) \times 10^{-6}$	^{145}Xe	$(3 \pm 1) \times 10^{-3}$
^{92}Kr	1.3 ± 0.4	^{115}Mo	$(5 \pm 3) \times 10^{-6}$	^{132}Cd	$(1.7 \pm 0.9) \times 10^{-6}$	^{146}Xe	$(4 \pm 1) \times 10^{-4}$
^{93}Kr	$(3 \pm 1) \times 10^{-1}$	^{107}Tc	17 ± 6	^{123}In	19 ± 7	^{147}Xe	$(9 \pm 5) \times 10^{-6}$
^{94}Kr	$(7 \pm 2) \times 10^{-2}$	^{108}Tc	8 ± 2	^{124}In	5 ± 2	^{140}Cs	4 ± 1
^{95}Kr	$(1.6 \pm 0.5) \times 10^{-2}$	^{109}Tc	4 ± 1	^{125}In	$3. \pm 1$	^{141}Cs	4 ± 1
^{96}Kr	$(3 \pm 1) \times 10^{-3}$	^{110}Tc	1.5 ± 0.5	^{126}In	1.6 ± 0.5	^{142}Cs	2.7 ± 0.9
^{97}Kr	$(1.2 \pm 0.4) \times 10^{-4}$	^{111}Tc	$(7 \pm 2) \times 10^{-1}$	^{127}In	1.1 ± 0.4	^{143}Cs	1.3 ± 0.4
^{92}Rb	5 ± 2	^{112}Tc	$(1.5 \pm 0.5) \times 10^{-1}$	^{128}In	$(2.8 \pm 0.9) \times 10^{-1}$	^{144}Cs	$(5 \pm 2) \times 10^{-1}$
^{93}Rb	4 ± 1	^{113}Tc	$(4 \pm 1) \times 10^{-2}$	^{129}In	$(1.2 \pm 0.4) \times 10^{-1}$	^{145}Cs	$(1.1 \pm 0.4) \times 10^{-1}$
^{94}Rb	2.1 ± 0.7	^{114}Tc	$(1.1 \pm 0.3) \times 10^{-2}$	^{130}In	$(3.0 \pm 0.9) \times 10^{-2}$	^{146}Cs	$(1.7 \pm 0.6) \times 10^{-2}$
^{95}Rb	1.2 ± 0.4	^{115}Tc	$(1.8 \pm 0.6) \times 10^{-3}$	^{131}In	$(7 \pm 2) \times 10^{-3}$	^{147}Cs	$(6 \pm 2) \times 10^{-3}$
^{96}Rb	$(3 \pm 1) \times 10^{-1}$	^{116}Tc	$(7 \pm 2) \times 10^{-5}$	^{132}In	$(9 \pm 3) \times 10^{-4}$	^{148}Cs	$(9 \pm 3) \times 10^{-4}$
^{97}Rb	$(8 \pm 3) \times 10^{-2}$	^{117}Tc	$(2.1 \pm 0.7) \times 10^{-5}$	^{133}In	$(1.8 \pm 0.6) \times 10^{-4}$	^{149}Cs	$(8 \pm 2) \times 10^{-5}$
^{98}Rb	$(1.8 \pm 0.6) \times 10^{-2}$	^{118}Tc	$(1.1 \pm 0.8) \times 10^{-6}$	^{134}In	$(8 \pm 3) \times 10^{-6}$	^{143}Ba	4 ± 1
^{99}Rb	$(4 \pm 1) \times 10^{-3}$	^{110}Ru	10 ± 3	^{126}Sn	6 ± 2	^{144}Ba	3 ± 1
^{100}Rb	$(1.0 \pm 0.4) \times 10^{-4}$	^{111}Ru	6 ± 2	^{127}Sn	3 ± 1	^{145}Ba	1.9 ± 0.6
^{101}Rb	$(1.4 \pm 0.7) \times 10^{-5}$	^{112}Ru	2.7 ± 0.9	^{128}Sn	2.5 ± 0.8	^{146}Ba	$(7 \pm 2) \times 10^{-1}$
^{94}Sr	12 ± 4	^{113}Ru	$(8 \pm 3) \times 10^{-1}$	^{129}Sn	1.4 ± 0.5	^{147}Ba	$(1.7 \pm 0.6) \times 10^{-1}$
^{95}Sr	6 ± 2	^{114}Ru	$(2.2 \pm 0.9) \times 10^{-1}$	^{130}Sn	1.0 ± 0.3	^{148}Ba	$(5 \pm 2) \times 10^{-2}$
^{96}Sr	4 ± 1	^{115}Ru	$(7 \pm 2) \times 10^{-2}$	^{131}Sn	$(4 \pm 2) \times 10^{-1}$	^{149}Ba	$(2.1 \pm 0.7) \times 10^{-2}$
^{97}Sr	2.0 ± 0.7	^{116}Ru	$(2.6 \pm 0.9) \times 10^{-2}$	^{132}Sn	$(4 \pm 1) \times 10^{-1}$	^{150}Ba	$(3.2 \pm 1) \times 10^{-3}$
^{98}Sr	(1.1 ± 0.4)	^{117}Ru	$(5 \pm 2) \times 10^{-3}$	^{133}Sn	$(5 \pm 2) \times 10^{-2}$	^{151}Ba	$(1.9 \pm 0.6) \times 10^{-4}$
^{99}Sr	$(2.6 \pm 0.8) \times 10^{-1}$	^{118}Ru	$(8 \pm 2) \times 10^{-4}$	^{134}Sn	$(1.2 \pm 0.4) \times 10^{-2}$	^{152}Ba	$(2 \pm 0.7) \times 10^{-5}$
^{100}Sr	$(9 \pm 3) \times 10^{-2}$	^{119}Ru	$(7 \pm 2) \times 10^{-5}$	^{135}Sn	$(9 \pm 3) \times 10^{-4}$	^{146}La	1.9 ± 0.6
^{101}Sr	$(1.5 \pm 0.5) \times 10^{-2}$	^{120}Ru	$(6 \pm 3) \times 10^{-6}$	^{136}Sn	$(1.3 \pm 0.4) \times 10^{-4}$	^{147}La	1.3 ± 0.4
^{102}Sr	$(2.1 \pm 0.7) \times 10^{-3}$	^{113}Rh	8 ± 3	^{137}Sn	$(5 \pm 2) \times 10^{-6}$	^{148}La	$(5 \pm 2) \times 10^{-1}$
^{103}Sr	$(1.1 \pm 0.4) \times 10^{-4}$	^{114}Rh	3 ± 1	^{129}Sb	5 ± 2	^{149}La	$(2.0 \pm 0.7) \times 10^{-1}$

TABLE II. *(Continued.)*

Isotope	Cross section (mb)	Isotope	Cross section (mb)	Isotope	Cross section (mb)	Isotope	Cross section (mb)
^{104}Sr	$(1.9 \pm 0.8) \times 10^{-5}$	^{115}Rh	1.8 ± 0.6	^{130}Sb	4 ± 1	^{150}La	$(4 \pm 1) \times 10^{-2}$
^{97}Y	11 ± 4	^{116}Rh	$(5 \pm 2) \times 10^{-1}$	^{131}Sb	4 ± 1	^{151}La	$(6 \pm 2) \times 10^{-3}$
^{98}Y	5 ± 2	^{117}Rh	$(1.8 \pm 0.6) \times 10^{-1}$	^{132}Sb	2.3 ± 0.7	^{152}La	$(7 \pm 2) \times 10^{-3}$
^{99}Y	4 ± 1	^{118}Rh	$(3 \pm 1) \times 10^{-2}$	^{133}Sb	1.4 ± 0.4	^{153}La	$(6 \pm 2) \times 10^{-4}$
^{100}Y	1.2 ± 0.4	^{119}Rh	$(1.6 \pm 0.5) \times 10^{-2}$	^{134}Sb	$(6 \pm 2) \times 10^{-1}$	^{154}La	$(3 \pm 1) \times 10^{-5}$
^{101}Y	$(6 \pm 2) \times 10^{-1}$	^{120}Rh	$(2.1 \pm 0.7) \times 10^{-3}$	^{135}Sb	$(1.4 \pm 0.4) \times 10^{-1}$	^{148}Ce	1.5 ± 0.6
^{102}Y	$(2.3 \pm 0.7) \times 10^{-1}$	^{121}Rh	$(2.9 \pm 0.9) \times 10^{-4}$	^{136}Sb	$(2.3 \pm 0.7) \times 10^{-2}$	^{149}Ce	$(8 \pm 3) \times 10^{-1}$
^{103}Y	$(5 \pm 2) \times 10^{-2}$	^{122}Rh	$(2.1 \pm 0.8) \times 10^{-5}$	^{137}Sb	$(1.5 \pm 0.5) \times 10^{-2}$	^{150}Ce	$(5 \pm 2) \times 10^{-1}$
^{104}Y	$(8 \pm 2) \times 10^{-3}$	^{123}Rh	$(3 \pm 1) \times 10^{-6}$	^{138}Sb	$(1.2 \pm 0.4) \times 10^{-3}$	^{151}Ce	$(1.7 \pm 0.6) \times 10^{-1}$
^{105}Y	$(8 \pm 2) \times 10^{-4}$	^{115}Pd	11 ± 4	^{139}Sb	$(1.3 \pm 0.4) \times 10^{-4}$	^{152}Ce	$(1.5 \pm 0.5) \times 10^{-1}$
^{106}Y	$(6 \pm 2) \times 10^{-5}$	^{116}Pd	5 ± 2	^{132}Te	6 ± 2	^{153}Ce	$(1.3 \pm 0.5) \times 10^{-2}$

[1] A. Jungclaus *et al.*, Phys. Rev. Lett. **99**, 132501 (2007).
[2] J. Benlliure *et al.*, Phys. Rev. C **78**, 054605 (2008).
[3] M. Bernas *et al.*, Phys. Lett. B **331**, 19 (1994).
[4] M. Bernas *et al.*, Phys. Lett. B **415**, 111 (1997).
[5] C. Engelmann *et al.*, Z. Phys. A **352**, 351 (1995).
[6] P. Armbruster *et al.*, Phys. Rev. Lett. **93**, 212701 (2004).
[7] J. F. Martin *et al.*, Eur. Phys. J. A **51**, 174 (2015).
[8] T. Ohnishi *et al.*, J. Phys. Soc. Jpn. **79**, 073201 (2010).
[9] N. Fukuda *et al.*, J. Phys. Soc. Jpn. **87**, 014202 (2018).
[10] Y. Shimizu *et al.*, J. Phys. Soc. Jpn. **87**, 014203 (2018).
[11] J. Cornell, Y. Blumenfeld, and G. Fortuna, Final report of the EURISOL Design Study (2005-2009) A Design Study for a European Isotope-Separation-On-Line Radioactive Ion Beam Facility, 2009, pp. 1–220, in2p3-00462950; http://hal.in2p3.fr/in2p3-00462950.
[12] K. Helariutta *et al.*, Eur. Phys. J. A **17**, 181 (2003).
[13] D. Pérez-Loureiro *et al.*, Phys. Lett. B **703**, 552 (2011).
[14] K.-H. Schmidt *et al.*, Nucl. Phys. A **665**, 221 (2000).
[15] J. Pereira, P. Armbruster, J. Benlliure, and K. H. Schmidt, Phys. Rev. C **75**, 044604 (2007).
[16] H. Geissel *et al.*, Nucl. Instrum. Methods Phys. Res., Sec. B **70**, 286 (1992).
[17] J. Pereira, J. Benlliure, E. Casarejos, P. Armbruster, M. Bernas, A. Boudard, S. Czajkowski, T. Enqvist, R. Legrain, S. Leray, B. Mustapha, M. Pravikoff, F. Rejmund, K. H. Schmidt, C. Stephan, J. Taieb, L. Tassan-Got, C. Volant, and W. Wlazlo, Phys. Rev. C **75**, 014602 (2007).
[18] R. Anne, A. Lefol, G. Milleret, and R. Perret, Nucl. Instrum. Methods **152**, 395 (1978).
[19] J. Benlliure, J. Pereira, and K.-H. Schmidt, Nucl. Instrum. Methods Phys. Res., Sec. A **478**, 493 (2002).
[20] P. J. Karol, Phys. Rev. C **11**, 1203 (1975).
[21] J. Benlliure *et al.*, Nucl. Phys. A **683**, 513 (2001).
[22] T. Enqvist *et al.*, Nucl. Phys. A **658**, 47 (1999).
[23] U. Brosa, S. Grossmann, and A. Müller, Phys. Rep. **197**, 167 (1990).
[24] C. Donzaud *et al.*, Eur. Phys. J. A **1**, 407 (1998).
[25] J.-J. Gaimard and K.-H. Schmidt, Nucl. Phys. A **531**, 709 (1991).
[26] A. Kelic, M. V. Ricciardi, and K.-H. Schmidt, arXiv:0906:4193v1.
[27] J. Benlliure *et al.*, Nucl. Phys. A **628**, 458 (1998).
[28] K.-H. Schmidt, A. Kelić, and M. V. Ricciardi, Europhys. Lett. **83**, 32001 (2008).
[29] K.-H. Schmidt *et al.*, Nucl. Instrum. Methods Phys. Res., Sec. A **260**, 287 (1987).
[30] E. Pellereau *et al.*, Phys. Rev. C **95**, 054603 (2017).
[31] J. P. Bocquet and R. Brissot, Nucl. Phys. A **502**, 213 (1989).
[32] G. Rudstam *et al.*, Radiochim. Acta **49**, 155 (1990).
[33] P. Fong, *Statistical Theory of Nuclear Fission* (Gordon and Breach, New York, 1969).
[34] M. G. Itkis, V. N. Okolovich, A. Ya. Rusanov and G. N. Smirenkin, Sov. J. Part. Nucl. **19**, 301 (1988).
[35] M. Asghar, Z. Phys. A **296**, 79 (1980).
[36] H. Nifenecker, J. Phys. Lett. **41**, 47 (1980).
[37] M. Bernas *et al.*, Nucl. Phys. A **725**, 213 (2003).